CFD modeling of condensing steam ejectors: Comparison with an experimental test-case

CFD modeling of condensing steam ejectors: comparison with an experimental test-case

Federico Mazzelli*, Francesco Giacomelli, Adriano Milazzo

Department of Industrial Engineering, University of Florence,

via di Santa Marta, 3 – 50139 FIRENZE (ITALY)

Abstract

In the present paper, a numerical model for the simulation of wet-steam flows has been developed and implemented within a commercial CFD code (ANSYS Fluent) via user defined functions. The scheme is based on a single-fluid approach and solves the transport equations for a homogeneous mixture coupled with conservation equations for the droplets number and liquid volume fraction. The model is validated against a steam nozzle test-case and then compared with experimental data from a steam ejector with a significant amount of generated liquid phase. The simulations show a good agreement both in terms of mass flow rates and pressure profile data. Some of the modeling assumptions are also reviewed and discussed.

Keywords: Wet-Steam; CFD; Experimental Test-Case; Steam Ejector; Non-Equilibrium Condensation

Nomenclature

Latin letters		*Greek letters*	
a	Speed of sound [m s^{-1}]	α	Volume fraction [-]
B	Second virial coefficient [m^3 kg^{-1}]	β	Mass fraction [-]
C	Third virial coefficient [m^6 kg^{-2}]	Γ	Liquid mass generation rate [kg m^{-3} s^{-1}]
c	Specific heat capacity [J kg^{-1} K^{-1}]	γ	Specific heat ratio [-]
G	Gibbs Free-Energy [J]	η	Droplets per unit volume mixture [m^{-3}]
h_{lv}	Latent heat [J kg^{-1}]	λ	Thermal conductivity [W m^{-1} K^{-1}]
J	Nucleation rate [s^{-1} m^{-3}]	ξ	Kantrowitz non isothermal correction
k_b	Boltzmann constant [J K^{-1}]	ρ	Density [kg m^{-3}]
k	Turbulent kinetic energy [m^2 s^{-2}]	σ	Surface tension [J m^{-2}]
l	Molecular mean free path [m]	τ	Shear stress [Pa]
m	Mass [kg]	φ_{ss}	Supersaturation ratio [-]
n	Droplets per unit mass of mixture [kg^{-1}]	ω	Specific dissipation rate [s^{-1}]

* Corresponding author: federico.mazzelli@unifi.it – 0039 055 2758740

p	Pressure [Pa]	*Subscripts*	
q_c	Accommodation factor	d	Droplet
R	Specific gas constant [J kg^{-1} K^{-1}]	m	Mixture, molecule
r	Radius [m]	v	Vapor
t	Time [s]		
T	Temperature [K]		
u	Velocity [m s^{-1}]		

1. Introduction

Non-equilibrium condensation of steam occurs in many jet and turbomachinery devices, such as supersonic nozzles, ejectors and low pressure stages of steam turbines. Normal operation of these devices involves flow expansions that leads to thermodynamic states that are well within the saturation dome. Due to the very limited residence time, however, thermodynamic equilibrium is not maintained and the water vapor reaches high levels of supercooling. At a certain degree of steam expansion, the vapor state abruptly collapses and condensation takes place as a shock-like disturbance, called the "condensation shock" [1]. This sudden change in the state of aggregation leads to an instantaneous and localized heat release that increases the pressure and temperature and reduces the Mach number. Moreover, the condensation shock implies large temperature differences between the phases that cause irreversibilities. Downstream of the condensation shock, the flow contains a considerable number of small liquid droplets (of the order of 10^{19}/dm^3, [2]) that can interact in non-trivial ways with the carrier phase.

To date, CFD simulations of wet-steam flows have proved to achieve a quite good agreement for the steam condensation within transonic nozzles [3], both in terms of pressure and droplet size trends. However, the same may not hold true in ejector applications where the interaction between droplets, shocks and shear layers may introduce many unpredictable effects. In this respect, most of the numerical studies on condensing steam ejectors have been accomplished through single-phase, ideal-gas simulations (e.g., [4]) and very few examples of CFD using wet steam models exist (see for instance, [5], [6]). This lack of detailed simulations of condensing steam ejectors provides motivations for this study.

In order to accurately validate numerical simulation on ejector applications, the comparison with experimental data should be made by considering both global and local parameters. Unfortunately, articles reporting these type of data appears to be very few. In particular, the study of Chunnanond and Aphornratana [7], and the subsequent work of Sriveerakul *et al.* [4], provide results for the entrainment ratios and pressure profiles along the ejector walls. However, no information on the separate primary and secondary mass flow rates is given, which makes difficult the assessment of numerical results. In this work, the validation of the developed model is made by comparing the simulation results against two different experimental test-cases, the converging-diverging nozzle from Moses and Stein [8] and the supersonic steam ejector studied by Al-Doori [9] and Ariafar *et al* [5], who provide data for both mass flow rates and wall pressure profiles.

2. Numerical Model

In the past decades, several methods have been devised to simulate wet steam flows, with different levels of complexities and accuracy. The simplest and perhaps most used is the so-called "single-fluid" approach. This is basically a fully Eulerian scheme that assumes the liquid phase to be uniformly dispersed within the vapor volume. The mass, momentum and energy conservation equations are written for the homogeneous two-phase mixture and two further equations describes the conservation of the droplets number and liquid mass within the computational domain. This method is commonly employed by commercial codes (e.g. ANSYS Fluent or CFX) and has been used by several research teams [5] [6] [10].

A second method, called the "two-fluid" approach, is very similar to the previous one, with the exception that the conservation equations are solved for the two phases separately. This can result in greater accuracy thanks to the possibility of describing the energy and force exchange between the phases. On the other hand, modeling the interphase interaction is a complex task that can potentially lead to larger uncertainties than with the use of simpler models (especially in ejectors, where the wet-steam flows across shear layers and shocks). The two-fluid method has been investigated by many authors, who have either adapted commercial codes [11] or developed in-house solvers [12] [13].

To date, wet steam models are available in many commercial CFD codes that generally feature models based on the single-fluid approach. Although these codes dispense from developing complex in-house solvers, the use of built-in models does not allow freedom in the change of model parameters and settings. This work represents an attempt to overcome this limitation through the development of a customized model within a widely used CFD commercial code. This approach has the double benefit of allowing great flexibility in the choice of the physical model and, at the same time, exploiting the capability of commercial software in terms of solver settings.

The scheme developed in this work is based on the single-fluid approach. The conservation equations for mass, momentum and energy are written for the average mixture fluid and assume the form of the conventional Navier-Stokes equations for compressible flows:

$$\begin{aligned}
&\frac{\partial \rho_m}{\partial t} + \frac{\partial \rho_m u_{mj}}{\partial x_j} = 0 \\
&\frac{\partial \rho_m u_{mi}}{\partial t} + \frac{\partial \rho_m u_{mi} u_{mj}}{\partial x_j} = -\frac{\partial p}{\partial x_j} + \frac{\partial \tau_{ij_eff}}{\partial x_j} \\
&\frac{\partial \rho_m E_m}{\partial t} + \frac{\partial \rho_m u_{mj} H_m}{\partial x_j} = \frac{\partial q_{j_eff}}{\partial x_j} + \frac{\partial u_{mi} \tau_{ij_eff}}{\partial x_j}
\end{aligned} \qquad (1)$$

In eq. (1), the properties of the mixture are described by means of mass or volume weighted averages:

$$\begin{aligned}
&\varsigma_m = \beta \varsigma_l + (1-\beta)\varsigma_v \\
&\chi_m = \alpha_l \chi_l + (1-\alpha_l)\chi_v
\end{aligned} \qquad (2)$$

where ς_m represents mixture thermodynamic properties like enthalpy, entropy, total energy, etc…, χ_m is the mixture density, molecular viscosity or thermal conductivity, β is the liquid mass fraction and α_l is the liquid volume fraction. The connection between these last two quantities is straightforward:

$$\beta = \frac{m_l}{m_l + m_v} = \frac{\alpha_l \rho_l}{\alpha_l \rho_l + (1 - \alpha_l)\rho_v} \qquad (3)$$

The evaluation of the mixture speed of sound requires special considerations [14], and is calculated here by means of an harmonic average:

$$a = \sqrt{\frac{1}{(\alpha_l \rho_l + \alpha_v \rho_v)\left(\frac{\alpha_l}{\rho_l a_l^2} + \frac{\alpha_v}{\rho_v a_v^2}\right)}} \qquad (4)$$

Coupled with the transport equation for the mixture are the two equations for the conservation of the liquid mass and the droplets number:

$$\frac{\partial \rho_m n}{\partial t} + \frac{\partial \rho_m u_{mj} n}{\partial x_j} = \alpha_v J \qquad (5)$$

$$\frac{\partial \rho_l \alpha_L}{\partial t} + \frac{\partial \rho_l u_{mj} \alpha_L}{\partial x_j} = \Gamma \qquad (6)$$

where "*n*" is the number of droplets per unit mass of the mixture and it is assumed that the two phases move at the same speed (no-slip condition).

The term *"J"* in eq. (5) represents the nucleation rate, i.e., the rate of formation of new droplets per unit volume of vapor and is expressed here through the classical nucleation theory (more details can be found in [15]) modified with the Kantrowitz non-isothermal correction [16]:

$$J = \frac{q_c}{(1+\xi)} \frac{\rho_v^2}{\rho_l} \left(\frac{2\sigma}{\pi m^3}\right)^{1/2} exp\left(-\frac{\Delta G^*}{k_b T_v}\right)$$
$$\xi = q_c \frac{2(\gamma - 1)}{(\gamma + 1)} \frac{h_{lv}}{R T_v} \left(\frac{h_{lv}}{R T_v} - \frac{1}{2}\right) \qquad (7)$$

Where q_c is the accommodation factor, h_{lv} is the liquid-vapor latent heat, σ is the liquid water surface tension and ξ is the Kantrowitz non-isothermal correction.

This correction is needed when the rapidity of the nucleation process prevents the two phase from reaching the thermal equilibrium (i.e., $T_L = T_v$). In the case of fast transformations (or low heat transfer rate between the

phases) the temperature in the cluster becomes greater than T_v due to the latent heat release. This localized heat release enhances the rate at which the molecules evaporate from the cluster surface and leads to a partial suppression of the critical nucleation rate J. The Kantrowitz' correction reproduces this phenomenon and typically reduces J by a factor of 50–100 [15].

The term ΔG^* in eq. (7) is Gibbs Free energy needed to form a stable liquid cluster (other thermodynamic constants are defined in the nomenclature). Thermodynamic stability considerations lead to a simple expression for ΔG^* [17]:

$$\Delta G^* = \frac{4}{3}\pi r^{*2}\sigma \qquad (8)$$

Where r^* is the critical radius of a stable liquid cluster:

$$r^* = \frac{2\sigma}{\rho_l R T_v \cdot ln\varphi_{ss}}$$
$$\varphi_{ss} = \frac{P_v}{P_{sat}(T_v)} \qquad (9)$$

where φ_{ss} is the supersaturation ratio.

Equations (7) - (9) give the rate at which liquid nuclei spontaneously form within the vapor stream. The presence of the exponential term in eq. (7) is indicative of the shock-like nature of the condensation phenomenon. Moreover, it is important to note that all the variables of equations (7) - (9) depend solely on the vapor thermodynamic state.

In order to close the set of governing equations, it is necessary to provide a law for the liquid mass generation rate per unit volume of mixture, Γ, in eq. (6). This quantity stems from two different sources:

$$\Gamma = \Gamma_{nuc} + \Gamma_{grow} = \alpha_v m_d^* J + \rho_m n \frac{dm_d}{dt} \qquad (10)$$

where m_d is the mass of a generic liquid droplet and m_d^* is its value when the liquid nucleus first forms. By assuming a spherical shape for all liquid droplets, these are given by:

$$m_d^* = \frac{4}{3}\pi\rho_l r^{*3}$$
$$m_d = \frac{4}{3}\pi\rho_l r_d^3 = \frac{\rho_l \alpha_l}{\rho_m n} \qquad (11)$$

The first of the two terms in the RHS of eq. (10) describes the mass generated from freshly nucleated droplets. This term is significant only in the first stages of the condensation process and is rapidly overtaken by the

second addendum, Γ_{grow}, which represents the growth or shrinkage of existing droplets. Its expression requires the definition of a droplet growth law. In this work we use the formulation derived by Hill following a statistical mechanics approach [2] and later rearranged by Young [18]:

$$\frac{dr_d}{dt} = \frac{p_v}{\rho_l h_{lv}\sqrt{2\pi R T_v}} \frac{c_p + c_v}{2} \cdot (T_s(p_v) - T_v) \qquad (12)$$

Equations from (1) to (12) form a closed system of equations that can be solved as long as the vapor and liquid equations of state and thermodynamic properties are provided. In this respect, calculations of the non-equilibrium phase-change of steam necessarily requires the description of the fluid properties in metastable conditions, meaning that common tabulated properties cannot be used to this purpose. Unfortunately, there is a serious lack of experimental data for the properties of steam in supercooled conditions, which is regularly testified by reports of the International Association for the Properties of Water and Steam (IAPWS) [19]. Consequently, it is necessary to extrapolate a generic equation of state outside its normal range of validity in order to describe metastable states within the saturation curve.

In the present work, the steam properties are calculated following the work of Young [20] who derived a Virial equation of state truncated at the third term of the expansion:

$$p = \rho_v R T_v \cdot (1 + B\rho_v + C\rho_v^2) \qquad (13)$$

where *B* and *C* are the second and third Virial coefficients. These are function of the sole temperature and their expressions were calibrated to match steam data in the range between 273.16 and 1073 K. Moreover, formulations for the enthalpy, entropy and specific heats are derived from the Virial equations based on a procedure described by Young [20]. The steam thermal conductivity and dynamic viscosity are given by low order polynomial functions of the vapor temperature obtained from interpolation of NIST dataset [21]. The liquid phase properties (viz., liquid density, specific heat capacity, thermal conductivity and viscosity) are calculated assuming saturation conditions and are again expressed through empirical correlations obtained from NIST [21]. Finally, the water surface tension is a function of the sole temperature and is expressed following Young [18].

The described model has been implemented within the commercial CFD package ANSYS Fluent v18.0 [22]. In this regard, ANSYS Fluent features a built-in Wet Steam model that exploits a specifically developed density based solver. Unfortunately, it is not possible to directly modify the nucleation rate and droplet growth laws of this model according to user defined schemes. Nevertheless, the set-up of a customized scheme is still possible within the framework of Fluent pressure-based multiphase solver by adding a number of User Defined Functions (UDF). Of these, three are needed to input the source terms for the liquid mass fraction and droplet number transport equation and to enforce the expression for the diameter of the droplets. Moreover, a User Defined Real Gas Model is required to implement the virial equation of state and transport properties of the

vapor phase. Ultimately, it may be worth to note that, although density-based solvers generally perform better, pressure-based schemes have also been successfully applied for the simulations of multiphase compressible flows with discontinuities (e.g. [23]). In the next section, the accuracy of the developed pressure-based scheme will be assessed by comparison with results from the Fluent density based model.

3. Steam Nozzle

In what follows, the presented numerical model is compared against data from the well-known nozzle test case of Moses and Stein [8]. The results are firstly also confronted with those obtained with the ANSYS Fluent built-in wet steam model in order to benchmark the present scheme with a previously validated code (e.g., [24] [25]). In this comparison, the droplet generation and growth rates equations implemented in the customized model are the same as those featured by the Fluent built-in scheme. Subsequently, we address the analysis of changes in some of the model's settings (e.g., the droplet growth law).

The computational domain for these simulations has approximately 30'000 quadrilateral cells with y+<1 along the nozzle surfaces and is presented in Fig. 1. Due to the relative simplicity of the flow field (e.g., absence of pressure shocks), it was possible to set-up a third order accurate QUICK scheme [26] for the spatial discretization of all transport equations. A k-ω SST turbulence model is selected for all simulations.

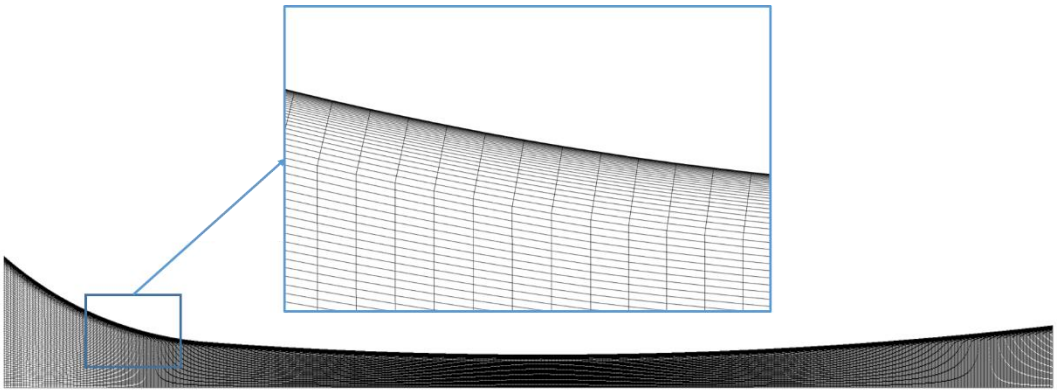

Fig. 1 – Computational domain for the nozzle test-case

Simulations are performed for the experiment n. 252, which has inlet total pressure of 40 kPa and inlet total temperature of 101.2 K [8]. For this test, data on pressure profiles and liquid mass fraction along the axis are available. Results on droplet average radius were not presented in the original paper; however, these were processed by Young [18] starting from light scattering data.

Fig. 2 shows the normalized pressure trend along the ejector axis. The figure focuses on the region downstream of the nozzle throat (located at x=8,22 cm from the nozzle inlet) where the condensation shock takes place and experimental measurements are available. Clearly, the presented model overlaps with results from the Fluent built-in model and both seem to capture the pressure trend with reasonable accuracy. When compared to

experimental values, numerical results underestimate the general pressure level and the steepness of the pressure rise.

Fig. 2 presents also the comparison on the average droplet radii along the nozzle axis. The results show that CFD predicts values that are approximately a half of the experimental. Nevertheless, it is known that for this particular test-case there is a general tendency to under-predict droplet sizes by CFD models [3].

It is interesting to note that the numerical trends for the average radius tend to predict different slope of the curve in the region where the nucleation has terminated. This difference is even more pronounced when comparing the trends for the number of droplets per unit volume of mixture, as shown in Fig. 3. The figure clearly shows two different trends of the numerical codes. In particular, the Fluent built-in model predicts the presence of a plateau immediately downstream of the nucleation zone, whereas the developed model shows a decreasing trend in this region.

The reason for this difference is to be found in the formulation for the droplet number conservation, eq. (5). In the present study, the equation is written in term of the conservation of the droplets per unit mass of mixture, which, once multiplied by the mixture density, returns the number of droplets per unit volume:

$$\eta = \rho_m n \qquad (14)$$

where η is the number of droplets per unit volume of mixture (or number density).

Writing eq. (5) in these terms allows the total number of droplets to be conserved in the computational domain, which is simply shown by performing a volume integration of the LHS of eq. (5) (the conservation of the droplet number can equally be obtained by using η as a variable, as long as the proper corrections to the droplet nucleation term, *J*, are made). Consequently, the present model improves on the Fluent built-in scheme by correctly reproducing a decreasing trend for η. This is caused by the fact that the total number of nuclei *n* is constant in this region (the nucleation rate is zero) and the flow is expanding in a duct with increasingly larger sections.

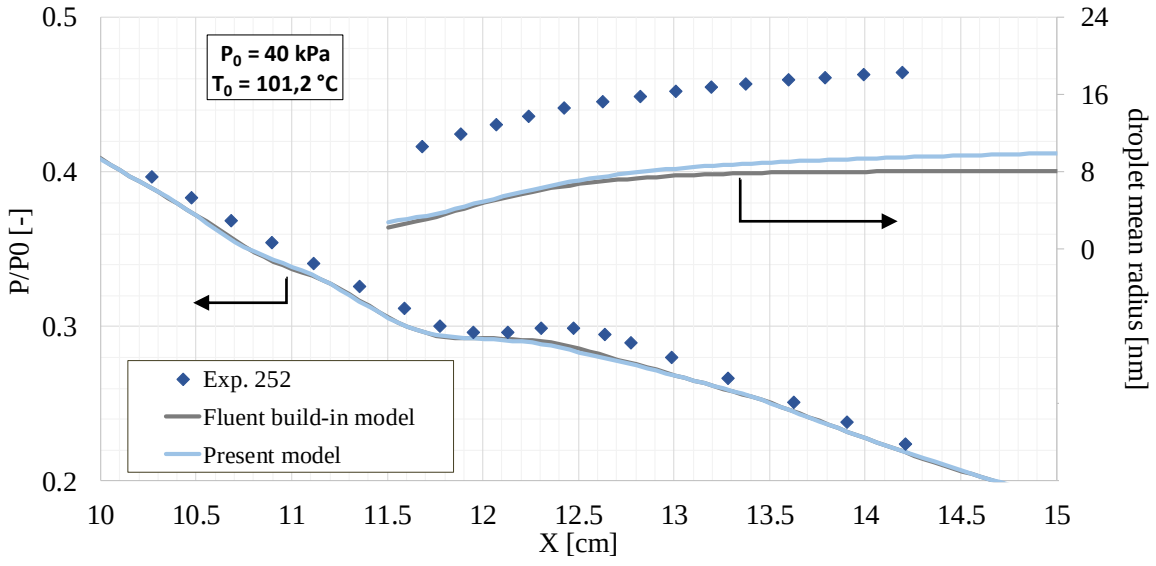

Fig. 2 – Normalized pressure trend along the nozzle axis (bottom curves) and corresponding droplet average radius (top right curves)

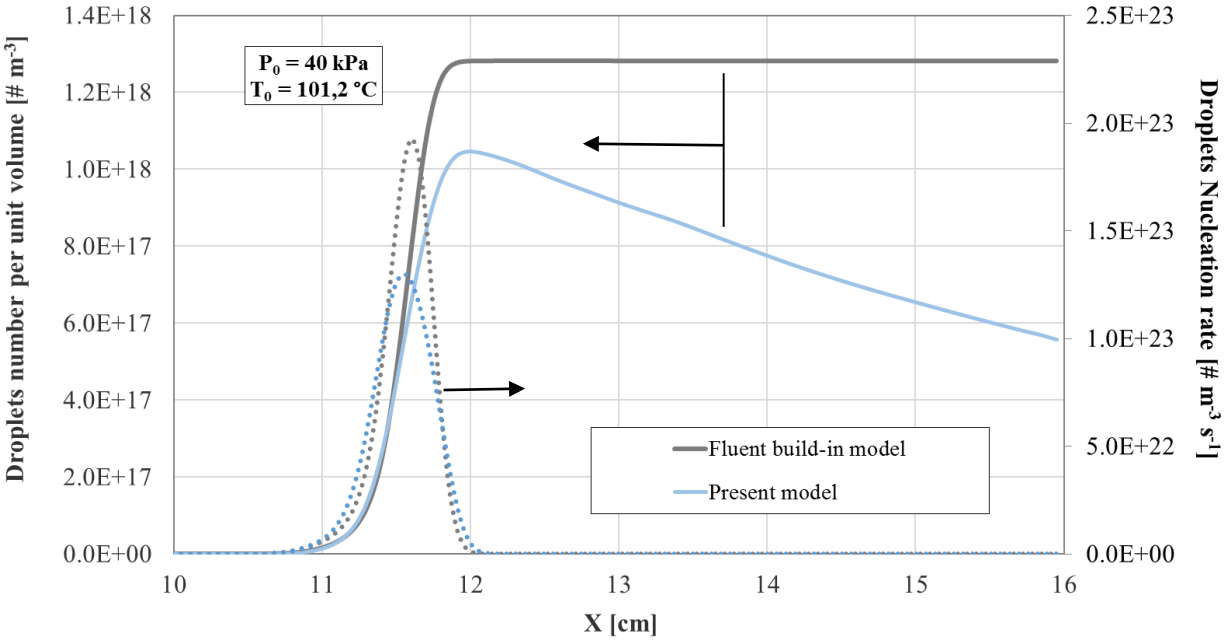

Fig. 3 – Number of droplets per unit volume of mixture along the nozzle axis (solid lines) and the corresponding droplets nucleation rates (dotted lines)

Sensitivity to different model settings

In this section, we present an analysis of the sensitivity to some of the most influential parameters of the phase change model, i.e., the surface tension, the nucleation equation and the droplet growth law. Specifically, we first evaluate the impact of suppressing the Kantrowitz non-isothermal correction from the nucleation equation. Secondly, we describe the surface tension by using an empirical correlation from IAPWS [19]. Lastly, we analyze the use of a widely used droplet growth law that was derived by Young [18] starting from an equation obtained by Gyarmathy [27]. Its final expression is as follows [3]:

$$\frac{dr_d}{dt} = \frac{\lambda_v}{\rho_l h_{lv} r_d} \frac{\left(1 - \frac{r^*}{r_d}\right)}{\left(\frac{1}{1 + 2C_1 Kn} + 3.78(1 - \upsilon)\frac{Kn}{Pr}\right)} \cdot (T_s(p_v) - T_v) \qquad (15)$$

$$\upsilon = \frac{RT_s}{h_{lv}}\left(C_2 - 0.5 - \frac{2 - q_C}{2q_C}\left(\frac{\gamma + 1}{2\gamma}\right)\left(\frac{c_p T_s}{h_{lv}}\right)\right) \qquad (16)$$

where λ_v is the vapor phase thermal conductivity, $Pr = \mu c_p/\lambda_v$ is the Prandtl number and *Kn* is the Knudsen number, defined as the ratio between the droplet diameter and the molecular mean free path:

$$Kn = \frac{l}{2r_d} \qquad (17)$$

The two constants C_1 and C_2 in eq. (15) and (16) represents two tunable modelling parameters (see [18] for a description of their significance) that are set respectively equal to 0.0 and 9.0, as suggested by Young [18].

Fig. 4 shows the comparison of the different model settings for four experimental cases (Exp. 252, 257, 193 and 411; for these last two measurements of the diameters are not available). Clearly, the use of the non-isothermal correction significantly retards the nucleation process with respect to the isothermal case. In turn, this results in a better agreement with experiments in all the simulated cases.

The adoption of the IAPWS correlation for the surface tension does not result in any detectable difference with respect to the formulation proposed by Young [18]. This is because the difference in the surface tension as predicted by the two correlations is always lower than 0.1% (at least for the range of temperature of interest for this study). However, it is important to note that both these formulation describes the surface tension as a function of the sole temperature and disregard any potential influence of the curvature radius.

Although it is generally acknowledged that the surface tension depends on the curvature for very small droplet radii (especially below 10nm [28], which is the range of interest for wet steam flows), experimental evidences are still required to specify how σ depends on r or even identify the sign of this variation (some studies suggest that this may be temperature-dependent, with a transition from positive to negative upon increasing T above ~250 K [28]). Moreover, due to its chief impact on the nucleation process (σ appears within the exponential term of eq. raised to the third power) any change in the expression for the surface tension most likely requires a complete recalibration of the physical model settings and constants. As a result, most of the previous works in the wet steam related literature have been accomplished exploiting the simplified flat-film surface tension assumption, as in this study.

Finally, the most interesting comparison in Fig. 4 relates to influence of the droplet growth law. The analysis of the various results reveals that the Young's droplet growth law can better capture the experimental trends for the average radius. By contrast, the two laws appear to alternatively match the experimental trends for the pressure, with the Young's law that always anticipate the nucleation region with respect to the Hill's expression.

This fact can be explained by considering the specific calibration adopted for the Young's droplet growth law. In particular, it is known that higher values of C_2 (as in this case) serve to boost the growth rate, resulting in larger droplets whilst simultaneously shifting the pressure rise upstream [3]. The analysis of other boundary conditions not reported here confirms the alternating performance of the two models. Therefore, it is not possible at present to draw a definite conclusion as to which model performs the best and both these expressions are tested for the analysis of the steam ejector.

Finally, it should be mentioned that the uncertainty connected to the pressure measurements was estimated by Moses and Stein [8] to be about ±40 Pa (the corresponding error bars are approximately of the same size of

the experimental symbols in Fig. 4). In terms of droplet radius, Starzmann et al [3] make reference to an estimated uncertainty of perhaps ±20%, although the details of the derivation are not reported.

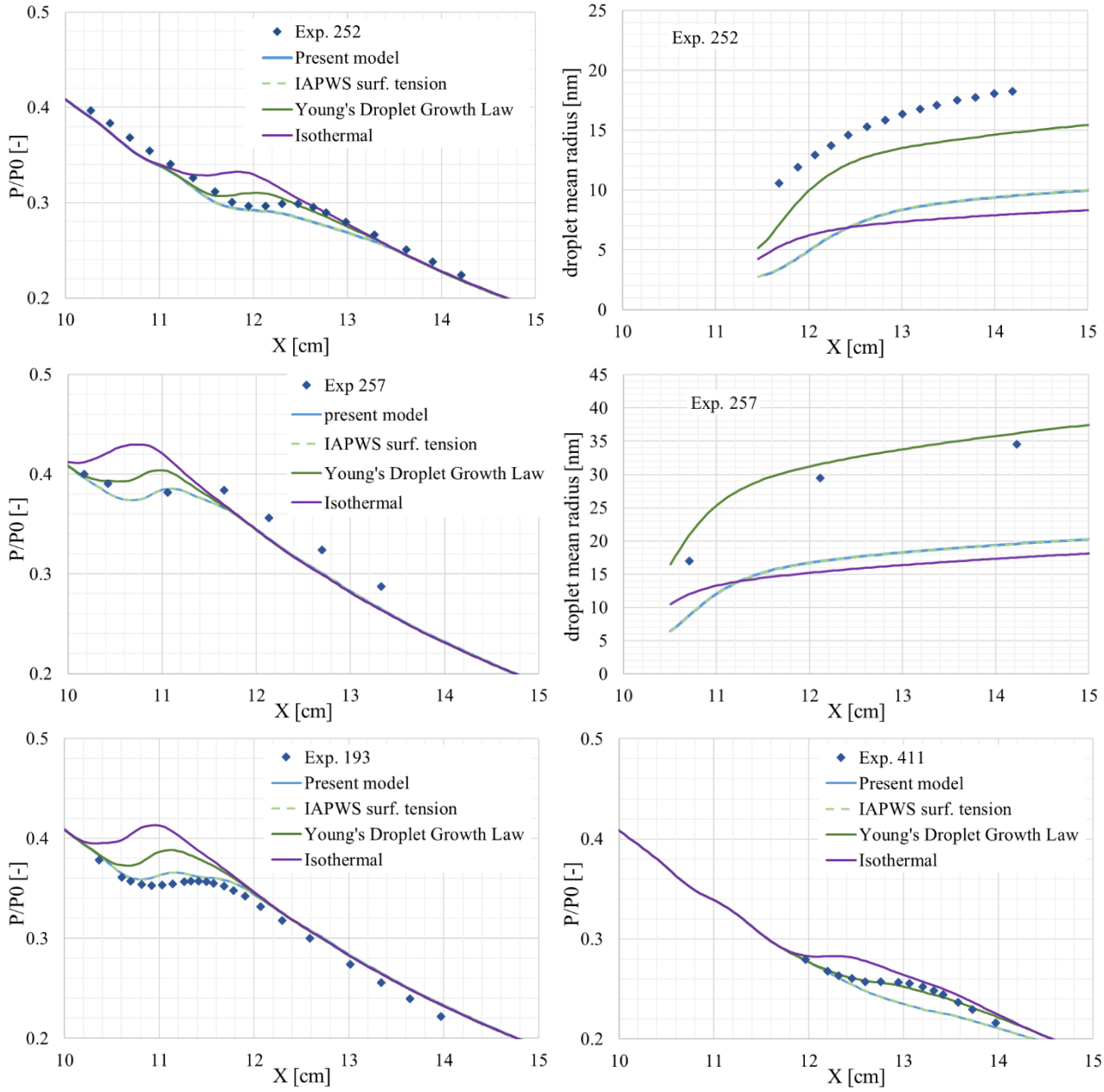

Fig. 4 – Comparison of model settings for different cases: Exp. 252 (P_0=40050 Pa, T_0=374.3 K), Exp. 257 (P_0=67661 Pa, T_0=376.7 K), Exp. 193 (P_0=43023 Pa, T_0=366 K), Exp. 411 (P_0=42276 Pa, T_0=385.15 K)

4. Steam Ejector

In this section, the developed model is validated against data from the supersonic steam ejector studied by Al-Doori [9] and Ariafar *et al* [5].

The set of boundary conditions analyzed are summarized in Table 1. The solution of the governing equations is achieved exploiting a pressure-based coupled solver. A second order accurate up-wind scheme is selected for the spatial discretization of all transport equations except for the volume fraction and momentum equations. The first of these is discretized through a 3rd order QUICK scheme whereas for the latter a power-law scheme had to be chosen due to numerical instabilities connected with the pressure-velocity coupling.

A k-ω SST turbulence model is selected for all the simulations because of the specific calibration for transonic applications [29] and based on previous studies on single phase ejector flows [30] [31]. In addition, due to the high Mach reached within the ejector mixing chamber, two additional UDFs are built to endow the turbulence model equations with the correction for compressible mixing layer (in ANSYS Fluent, these are available only for single-phase flows).

Table 1: Summary of ejector boundary conditions

Stream	Total Temperature [K]	Total Pressure [kPa]
Motive	403	270
Suction	287	1.6
Discharge		From 4.2 to 7.5 static pressure

Fig. 5 shows the computational domain used for all the CFD analyses. Due to the high directionality of the flow (axial velocity component always greater than transversal component), a structured grid is selected to reduce numerical diffusion. Moreover, a straight channel is added at the end of the domain, due to the presence of large recirculation regions at the ejector outlet that prevented reaching stable convergence for some operating conditions. Although this change may induce some approximations, these are most probably limited to a small region near the outlet (the flow upstream of the shock in the diffuser is not influenced due to the hyperbolic nature of the supersonic flow). Moreover, the inclusion of the channel prevents backflow of unknown characteristics from entering into the ejector and allows the recirculation to reattach within the computational domain, thus improving the numerical stability of the simulations.

The adequacy of the mesh refinement was checked by comparing the mass flow rates results for three different grids having all y+ values less than 1 along the ejector surfaces. Table 2 shows the results of the study. In order to reduce the computational time, the grid with 70k quadrilateral cells is selected for all subsequent calculations.

Convergence of the solution is defined by an error in the mass flow imbalance of less than 10^{-5} kg s^{-1} and calculations are stopped when all residuals are stable. Walls are assumed to be adiabatic and smooth.

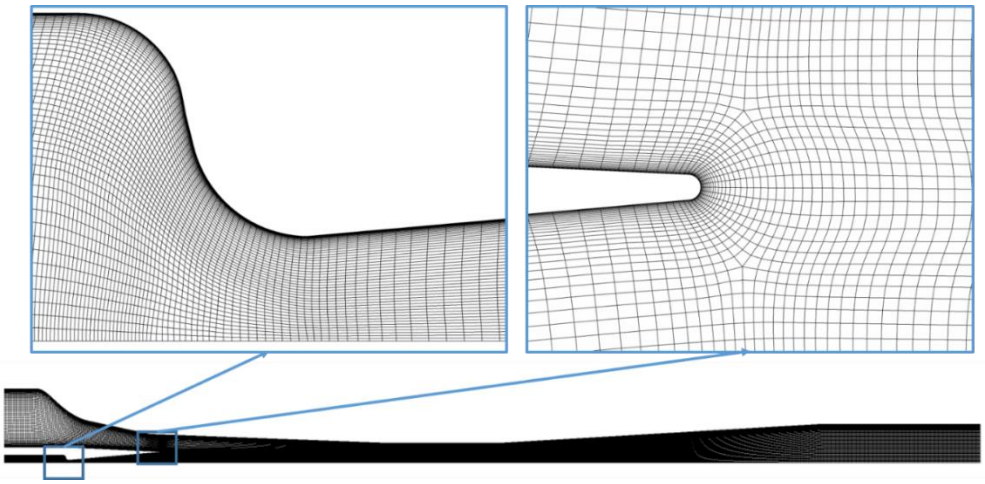

Fig. 5 – Computational domain and mesh details of the primary nozzle throat and fillet (grid with 70k cells)

Table 2: Grid independence study

Grid cells	Mass flow rate [kg/s]			Difference with finer mesh		
	Motive	Suction	ER	Motive	Suction	ER
~35 000	0.00341	0.00111	0.327	0.5%	-13.0%	-13.4%
~70 000	0.00339	0.00128	0.377	0.1%	1.2%	1.1%
~140 000	0.00338	0.00126	0.373	-	-	-

Entrainment Ratio and mass flow rates

Fig. 6 shows the comparison between the experimental and numerical Entrainment Ratio (ER) curves. Both the Young's and Hill's droplet growth law are tested (hereafter referred as Yg82 and Hi66). Details of the experimental apparatus and measurement procedures can be found in [9] (chapter 4 and 5). According to Al-Doori [9] the uncertainty level for the ER is around ±3%. The numerical simulations produce a higher value of ER at on design with a percent difference of about 14%. Moreover, CFD models somewhat anticipate and smoothen the transition toward the off design regime.

Despite the large discrepancy, Fig. 7 illustrates that when results for the motive and suction flows are analyzed separately, differences are smaller than the corresponding value of ER. This is due to a summation of the errors when dividing the two quantities (in other studies, the authors have found that the discrepancy was lower for the ER than the mass flow rates, as in [30]). In particular, the greatest discrepancy is achieved for the data of the suction flow rates, with a percent difference of about 7% at on design, whereas the difference for the motive flow rate is slightly less than 6%. For these two quantities, Al-Doori [9] reports uncertainties of 0.6% and 1-2% for the primary and secondary mass flow rate, respectively.

In terms of models sensitivity, the change of the droplet growth law seems to have a limited influence on the ejector mass flow rates. The only minor change occurs at off design, where the Hill's model performs slightly better than the Young's law. Moreover, a check of many flow variables has revealed only minor differences between the two models, as illustrated in Fig. 8 for the volume fraction and Mach profile along the ejector

axis. Consequently, all the subsequent analyses in this paper are carried out by considering only the Hill's droplet growth expression.

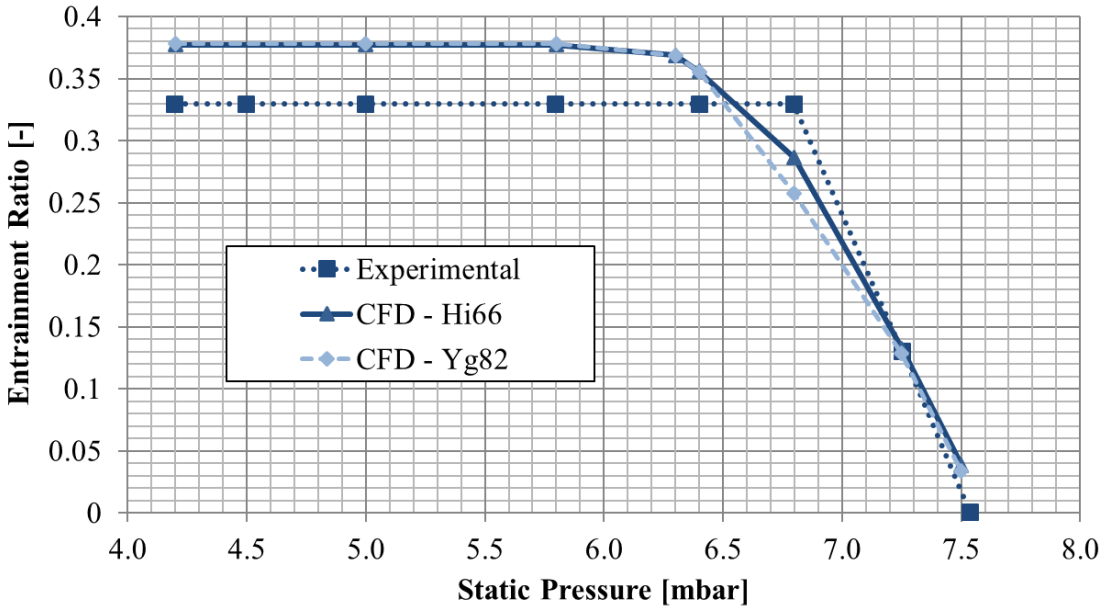

Fig. 6 – Comparison of experimental and numerical ER (experimental data are taken from [9])

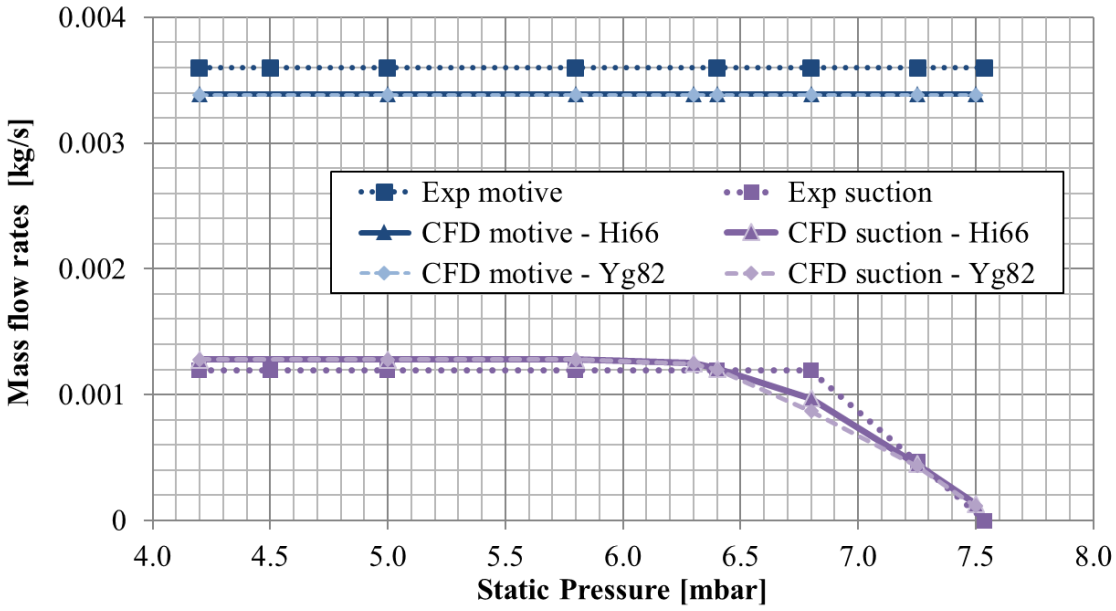

Fig. 7 – Comparison of experimental and numerical mass flow rates (experimental data are taken from [9])

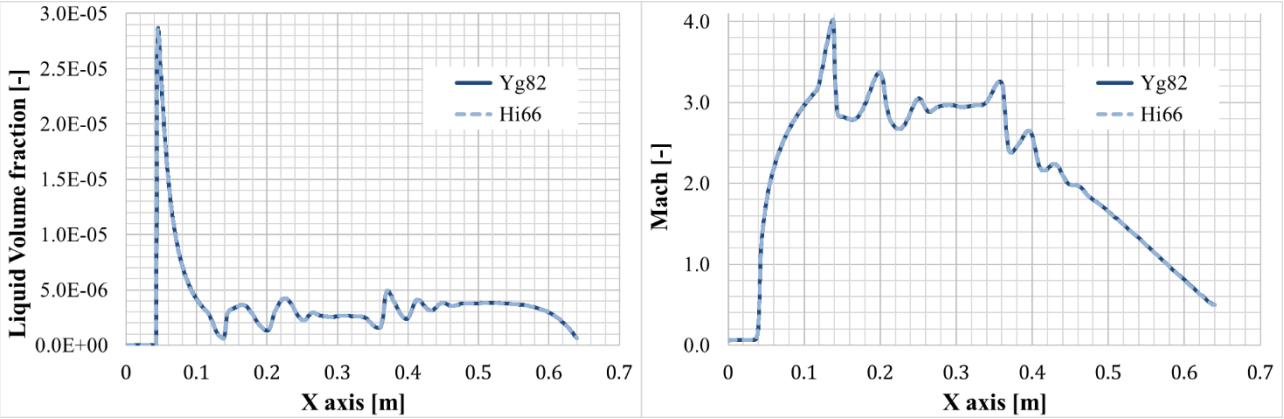

Fig. 8 – Liquid Volume Fraction (left) and Mach Number (right) profiles along the ejector axis. Comparison of different droplet growth models (P_{out} = 4.2 kPa)

Accuracy of mass flow rates predictions

Despite the general trend for ER being well reproduced, the discrepancy on the primary flow rate is still large compared with the error that should reasonably arise from the simulation of the 1D flow across a De Laval nozzle. A first possible cause for this discrepancy may come from numerical inaccuracies due to the low grid refinement and low order discretization (especially for the momentum equation). In order to check this hypothesis, a grid/order independence was performed solely on primary nozzle and the results are shown in Table 3. Clearly, despite some differences between the low and high order schemes remaining even for the finest mesh, the scatter is in all cases well below the 1%.

One further reason for the discrepancy of the primary flow rate may be the presence of liquid at motive inlet (it should be noted that no superheating was imposed in the experimental tests). This may increase the average density of the stream passing through the throat, producing a larger value of experimental flow rate. Moreover, the presence of liquid nuclei or steam impurities (such as solid particles) may strongly affect the intensity and type of the condensation process (see for instance [12]). In this respect, a sensitivity analysis was performed by varying the amount of liquid mass fraction at nozzle inlet (the simulations were performed for the 22k nozzle mesh with the 3 order accurate scheme). The results of these trials showed that in order to increase the motive mass flow rate of about 6%, it is necessary to impose nearly 15% of liquid mass fraction at inlet[1], which is a too large amount to explain the discrepancy with experiments. Nevertheless, these trials were performed with the single-fluid approach described previously. This method is generally not suited to investigate problems with secondary or multiple nucleation [32]; hence, the obtained results cannot exclude the presence of liquid nuclei at the motive inlet, which could have an impact on the experimental trends.

Finally, one further cause may be the uncertainty connected with the experimental measurements and with the geometrical dimension of the throat. As for the first, Al-Doori [9] estimates an uncertainty of around 0.6% for the primary mass flow rate, which is almost one order of magnitude lower than the differences with CFD. On

[1] This indicates that change in flow rate does not linearly depend on density variations, for instance, adding 6% percent of mass fraction at inlet leads to an increase of around 1.5% of the primary flow rate

the other hand, previous studies performed on a single phase air ejector [30] have shown that even small uncertainties in the throat dimension (connected mostly with the manufacturing process), can lead to discrepancies in the mass flow rate up to many percents. Unfortunately, Al-Doori does not report information on the geometrical uncertainty and manufacturing precision for the investigated profiles. Nevertheless, a first estimation of the sensitivity to the nozzle throat diameter can be achieved by making use of the compressible 1D equations for perfect gases.

By considering an average specific heat ratio of 1.3 (as found from inspection of CFD results), this method returns a primary mass flow rate ~ 0.00336 kg/s, which is around 1% lower than CFD results. By making use of this simple approach, it is found that an increase of only 16 μm (i.e., 1% of the nominal diameter) produce a change of the mass flow rate of more than 2%. If we consider this estimated sensitivity to approximately hold for CFD simulations, it follows that a discrepancy of around 50 μm may provide a difference close to the one obtained in the present simulations.

It is concluded that both the presence of liquid at inlet and possible geometrical uncertainties may have played a role in the observed differences with experimental primary flow rate.

Table 3: Motive nozzle mass flow rates for different grid size and discretization schemes

Grid size \ Discr. order	1st order	Present setup	Full 2nd order	3rd order
~22 000*	3.388 E-03	3.388 E-03	3.369 E-03	3.371 E-03
~44 000	3.376 E-03	3.378 E-03	3.363 E-03	3.365 E-03
~88 000	3.376 E-03	3.376 E-03	3.357 E-03	3.357 E-03

*this is the mesh size used for the ejector calculations

We focus now on the suction flow rate. From a general viewpoint, it is known that accurate predictions of the entrainment process requires accounting the influence of compressibility on the mixing layer. In particular, experimental investigations performed in the 70s (e.g., [33] [34]) have shown that compressible mixing layers are affected by a significant reduction of the spreading rate with respect to equivalent low-speed configurations.

Although this effect has been known for a long time, no convincing theoretical explanation has been given yet and turbulence models predict this decrease empirically (see Smits and Dussauge [35] or Gatsky and Bonnet [36] for more details). For ω-based models, Wilcox [37] proposes a correction to the turbulence kinetic energy equation based on the turbulent Mach number:

$$Ma_t = \frac{\sqrt{2k}}{a} \qquad (18)$$

where k is the turbulent kinetic energy and a is the speed of sound.

The compressibility correction reduces the mixing layer entrainment by increasing the dissipation of turbulence kinetic energy within shear layers. Although its use improves the accuracy for compressible mixing

layers, the correction can negatively affect predictions for wall boundary layers at transonic and supersonic speeds [38]. Because of this, the application of the correction was carefully evaluated.

Fig. 9 shows a comparison of the turbulent Mach number field between a simulation with the compressibility correction active and one without correction. As can be seen, the turbulent Mach reaches very high levels within the mixing layer and downstream of the shock in the diffuser. In particular, a substantial part of the mixing layer presents values of Ma_t larger than 0.25, which is the threshold for compressibility to have any impact on the mixing layer [38]. The use of the correction limits these peak values and reduces the mixing layer spreading rate. In turn, the suppression of the spreading rate results in a reduction of the suction flow rate of nearly 17% percent. Therefore, the difference with the experimental mass flow rate would be of about 22% without the compressibility correction (as opposed to the 7% obtained with the correction).

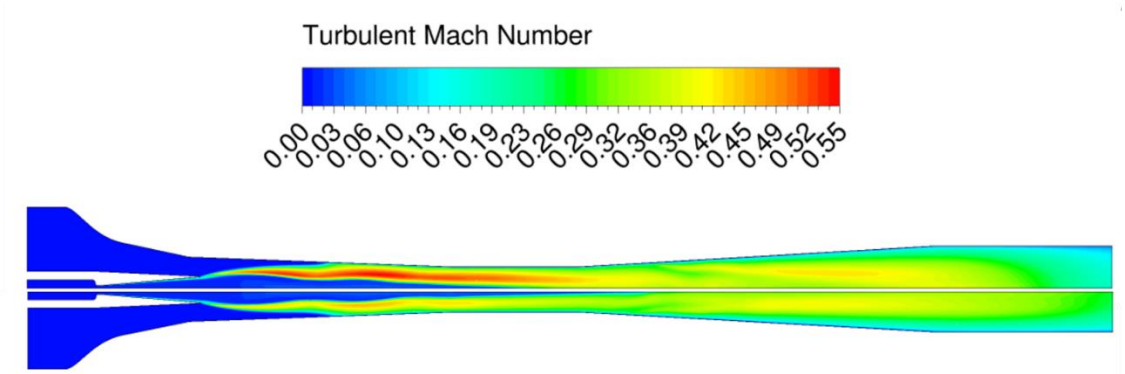

Fig. 9 – Turbulent Mach number contour for the case with compressibility correction (bottom) and without compressibility correction (top) (P_{out} = 4.2 kPa)

Wall Pressure Profile

Fig. 10 presents the results for the pressure profiles along the ejector wall. In order to perform the comparison, the outlet boundary conditions were imposed so as to match the value of the last pressure probe in the diffuser. This was necessary due to the presence of large recirculations along the diffuser that prevented the pressure recovery from completing at the ejector outlet (it should be noted that the straight channel attached downstream of the diffuser begins at *x= 535.5 mm*).

Overall, the comparison with experimental data shows a good agreement, especially near the mixing chamber entrance and throat regions. The accord with experiments decreases as flow approaches the diffuser, where the recirculations are found. These are notoriously hard to capture by common two-equation turbulence models and could partly account for the differences with experiments. Furthermore, the discrepancies in the prediction of the mass flow rates may also impact the results for the pressure trends. This is because the energy budget of the total stream is altered due to the different proportions of motive and suction flows, changing the positions of the shock within the diffuser as well as the pressure recovery trends.

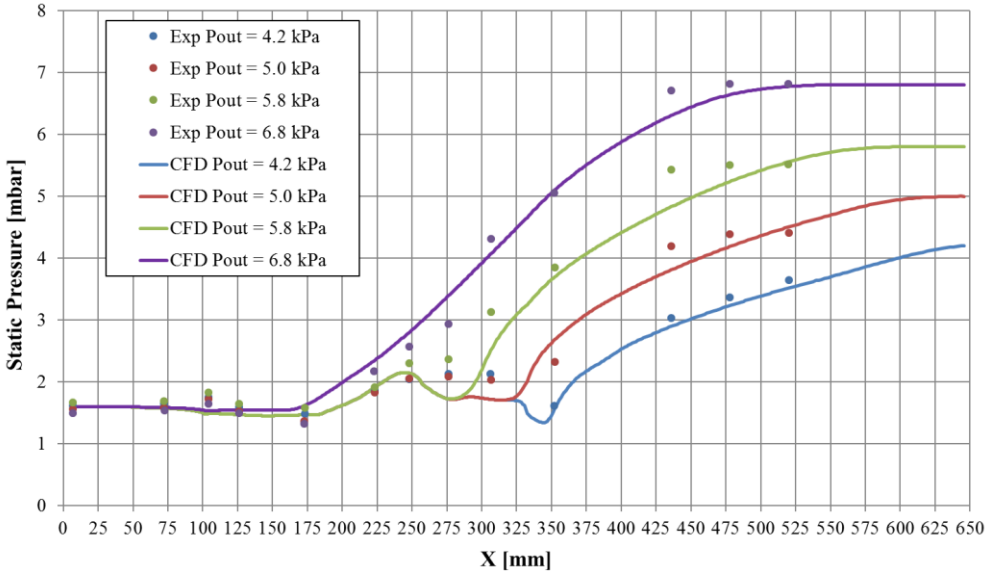

Fig. 10 – Comparison of experimental and numerical wall pressure profiles (experimental data are taken from [9])

Fig. 11 and Fig. 12 show the flow recirculation patterns and shock train structures for the different outlet pressures. It is interesting to note that the case with the lowest outlet pressure present a flow pattern that consists of two different vortex structures. A first one, smaller, occurs right after the shock train in the diffuser, and a second, larger, farther downstream. This case also presents the best agreement with the experimental pressure trend. According to CFD, the patterns adjust to a single vortex structure when the outlet pressure is increased. However, the agreement with experiments is reduced, therefore, these numerical patterns should be considered with some caution. Finally, the numerical Schlieren contours in Fig. 12 show that the pressure-based scheme adopted in this work can qualitatively reproduce the shock train structures within the ejector. However, the thickness of each shock may be overestimated due to the higher numerical diffusion of these schemes.

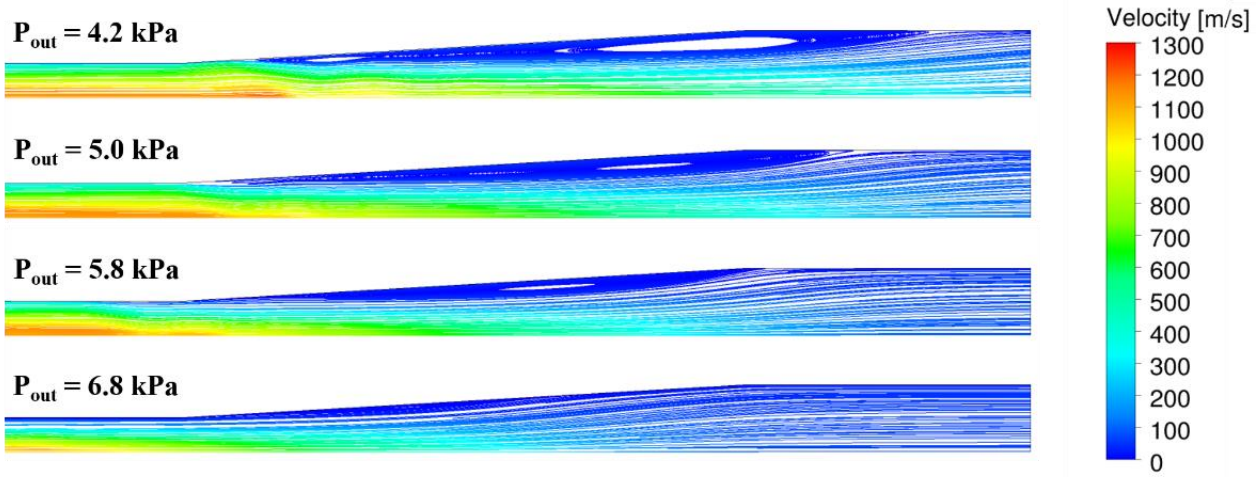

Fig. 11 – Streamline pattern at the ejector outlet showing the recirculation regions

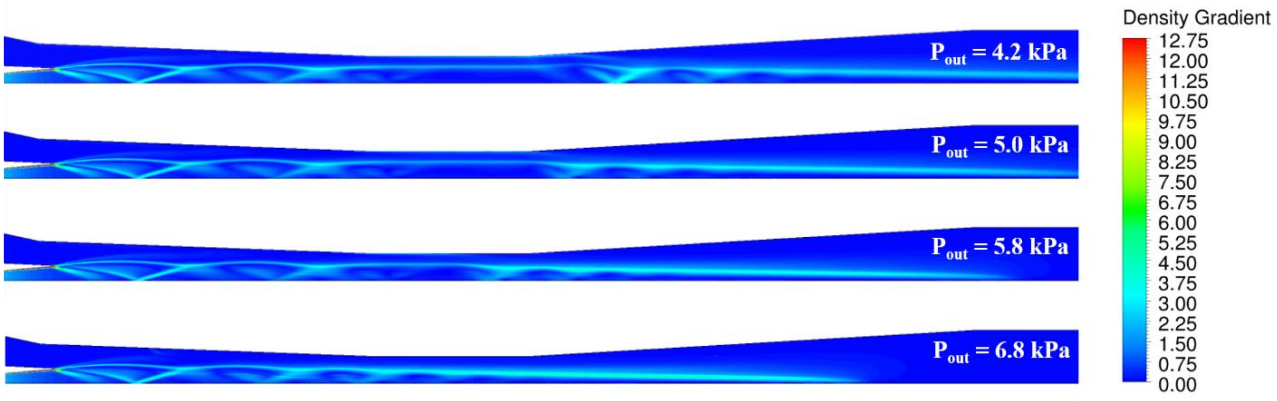

Fig. 12 – Numerical Schlieren images (density gradient contours) showing the shock train structures

Two-phase flow features

Fig. 13 shows the contour of the liquid mass fraction for the case with the lowest outlet pressure (P_{out} = 4.2 kPa). As can be seen, the condensed phase reaches value up to 20% of the total mass, with peak levels in the region downstream of the nozzle exit plane. This is due to the further acceleration caused by the primary jet under-expansion. The absence of any superheating of the motive stream exacerbate this problem that can lead, in some extreme cases, to the formation of ice inside the ejector (as discussed in the next section).

Fig. 13 further illustrates that the liquid mass fraction evaporates almost completely toward the ejector outlet, where the mixed stream undergoes the shock trains and decelerate to reach the outlet pressure. In addition, the liquid mass fraction goes to zero at the nozzle wall, due to the heat recovery caused by the fluid deceleration and viscous dissipation within the boundary layer [1].

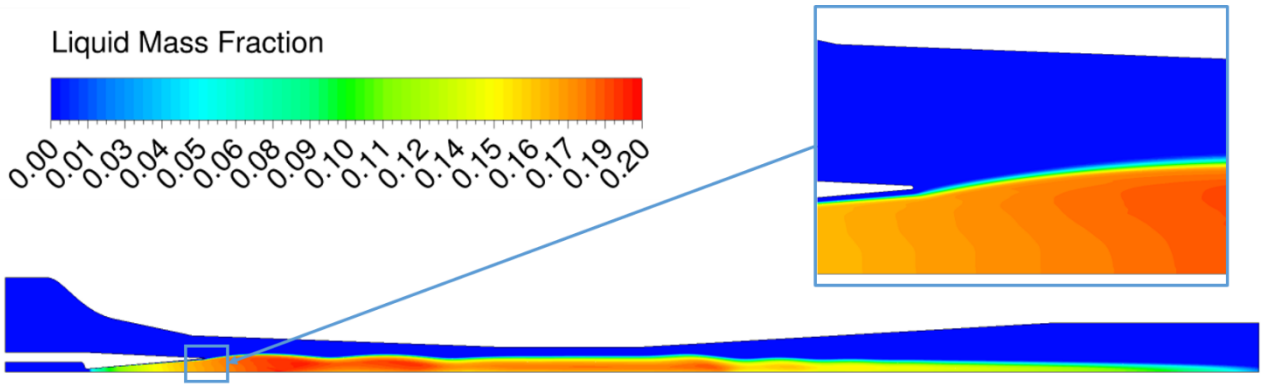

Fig. 13 – Liquid mass fraction contour (case with P_{out} = 4.2 kPa)

Fig. 14 shows the contour of the droplet number per unit mass of mixture, *n*. The figure displays also the line representing the boundary where the liquid mass fraction is zero.

The contour clearly reveals the presence of a radial distribution of the droplet number. This stems from the significant curvature of the nozzle profile at the throat, which induces a region of low pressure near the wall

and causes a stronger nucleation. The nucleated droplets are then convected down the ejector along streamlines and the radial distribution persist almost unaltered till the outlet.

The analysis of Fig. 14 further shows that the droplets number contour follows closely that of the liquid mass fraction depicted in Fig. 13. This is a direct consequence of the assumption of equal velocity between the phases. Yet, the comparison reveals also that toward the ejector outlet, where the condensed mass evaporates completely, the liquid droplets do not disappear but survive in the form of nuclei with zero mass and volume. The reason for this numerical error is to be found in the absence of a "droplets sink" term within the droplet transport equation, eq. (5).

This is a common feature of the single-fluid approaches which partly prevent their use in applications where secondary nucleation occurs (e.g., multi-stage steam turbine cascades). Although in principle it could be possible to add a sink term to the droplet number equation, in practice, the differential nature of the droplet transport equation complicates this task. For instance, the inclusion of a negative sink term in eq. (5) leads to regions with negative numbers of droplets. This problem may be worked around by positively limiting the value of the droplet number. Unfortunately, this is not possible in ANSYS Fluent.

Other options may exist in which, for instance, the value of the sink term is related to the number of droplets existing in the cell or it is described on a logarithmic basis. To the authors' knowledge, these approaches have never been attempted before and may require an extensive development work. However, this effort may not be completely justified in view of the fact that the assumptions implicit in the single-fluid approach would anyhow lead to significant approximations (e.g., the droplet sizes originating from different nucleation sites are averaged out). In this respect, the adoption of more advanced schemes, such as the multi-fluid approach mentioned in the introduction or a Lagrangian approach (e.g., [32]), naturally account for the removal of droplets from the computational domain and can provide more accurate results than the method used in this work.

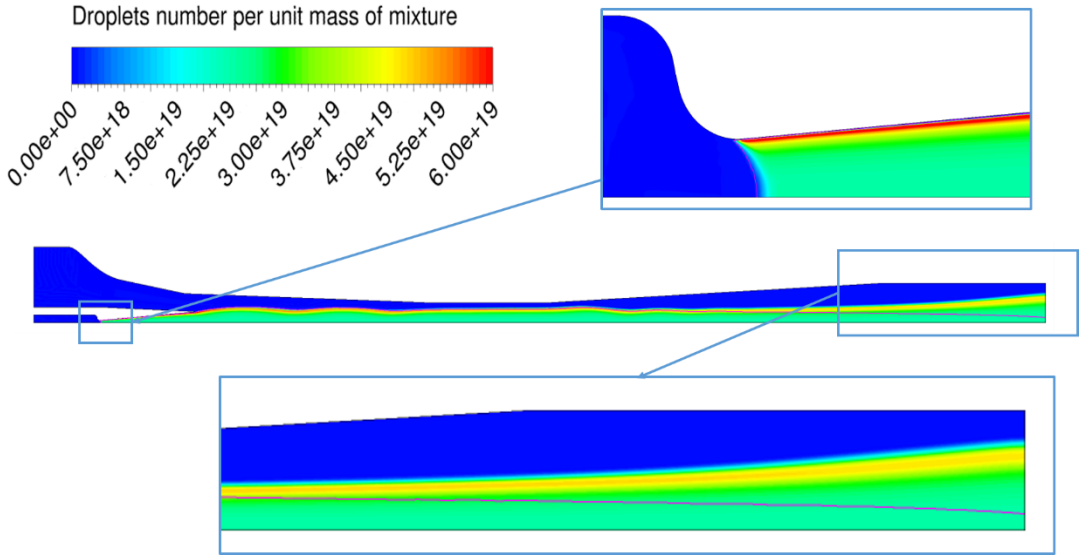

Fig. 14 – Contour of the droplet number per unit mass of mixture (in purple is the line where the liquid mass fraction is zero; case with P_{out} = 4.2 kPa)

Model limits

In this final section, we would like to review certain specific limits connected with the developed model and discuss possible implications deriving from them. In doing so, we focus on those assumptions that seem particularly restrictive with respect to steam ejector applications.

A first limit connected with the developed model relates with the droplet growth regime. Generally speaking, the growth rate formulation for a liquid droplet is calculated differently depending on value of the Knudsen number. During the initial phase of the droplet growth, the liquid nucleus is generally much smaller than the mean free path, i.e., $Kn>>1$. Under these conditions, named as *free molecular regime*, the continuum hypothesis does not hold and the calculation of the droplet growth must be accomplished by means of kinetic theory or statistical mechanics concepts. At the other extreme is the situation where $Kn<<1$. In this case the droplet is large enough to apply the macroscopic balances for heat, mass and momentum. In between these two conditions is what is called the transition regime ($Kn\sim1$). This is the most difficult to analyze and is usually handled by means of interpolations formulae that connect the continuum and free molecular regimes (see for example [18]).

Specifically, the Hill's droplet growth law adopted in this work is valid only for the free molecular regime, so that some questions may arise about its applicability to ejector flows (especially in the case of under-expanded nozzles with a delayed appearance of shocks that can vaporize or reduce the droplet dimensions [1]).

Fig. 15 shows the trend of the Knudsen number along the ejector axis, for one of the simulated cases (but all cases present similar trends). Clearly, the value of Kn is always well above unity except for a very small region near the primary nozzle throat. In this zone, the vapor temperature is still high and the mean free path is of the same order of magnitude of the droplet diameters (around 10^{-9} m).

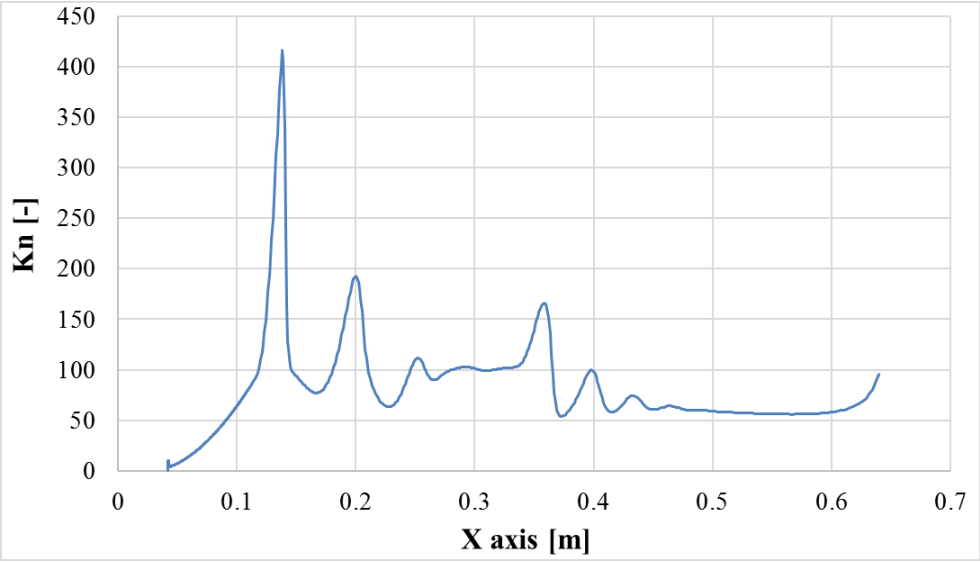

Fig. 15 – Knudsen number trend along the ejector axis (case with P_{out} = 4.2 kPa)

Somewhat connected with the issue of the droplet growth regime is the assumption of velocity equilibrium between the phases. In order to understand whether a particle will follow the gaseous stream trajectory or depart from it, it is possible to estimate the Stokes number related with the particle velocity [39].

The Stokes number is defined as the ratio between the droplet response time to a variation in the velocity field and a flow characteristic time of the continuous phase:

$$St = \frac{t_d}{t_v} \qquad (19)$$

When the Stokes number is much lower than unity, the condensed phase will closely follow the gaseous stream and it is allowed to assume a common velocity between the phases, as in the present work.

The droplet response time depends on the condensed phase inertia and on the carrier phase viscosity [39]:

$$t_d = \frac{\rho_d D_d^2}{18\mu_v} \qquad (20)$$

The carrier phase time can be calculated as the ratio between a characteristic velocity and length scale:

$$t_v = \frac{u_v}{L} \qquad (21)$$

Clearly, the definition of this last quantity is somewhat arbitrary because no specific definition of the characteristic length is provided. For nozzle flow, this is often the throat diameter, the use of which would give an estimate of St ~10^{-3}. However, this result refers to a characteristic time representative of the mean flow and does not consider any possible velocity mismatch arising from the interaction between turbulence and the dispersed phase. To this aim, t_v can be chosen so as to represent a turbulent characteristic time. Specifically, it is possible to calculate the Stokes number by using the inverse of the specific dissipation rate, which represents the frequency of the smallest turbulent eddies (those occurring at the Kolmogorov scale), i.e.:

$$t_v = t_{turb\_min} = \frac{1}{\omega} \qquad (22)$$

where ω is the specific dissipation rate.

Fig. 16 shows a map of this "turbulent" Stokes number within the ejector. Clearly, the assumption of equilibrium velocity appears to be satisfied in the whole two-phase flow domain, meaning that the fluid particle velocity should follow not only the average flow trajectories, but also the path of the smallest turbulent eddies (those with the highest frequency).

However, it should be noted that the above Stokes number was calculated under the assumption of "smooth" flow conditions. The presence of any local perturbation may notably reduce the characteristic length, which,

in the specific case of a dynamic shock, is generally of the same order of magnitude of the molecular mean free path. In this case, the different inertia between vapor and liquid droplets may produce a local velocity mismatch and lead to the departure of the phase trajectories. Moreover, the effects of drag and interphase momentum exchange has been neglected in this work although it could represent a non-negligible source of kinetic energy losses. Detailed analyses of these type of processes is a complex task and may require the use of more advanced models than the single-fluid approach.

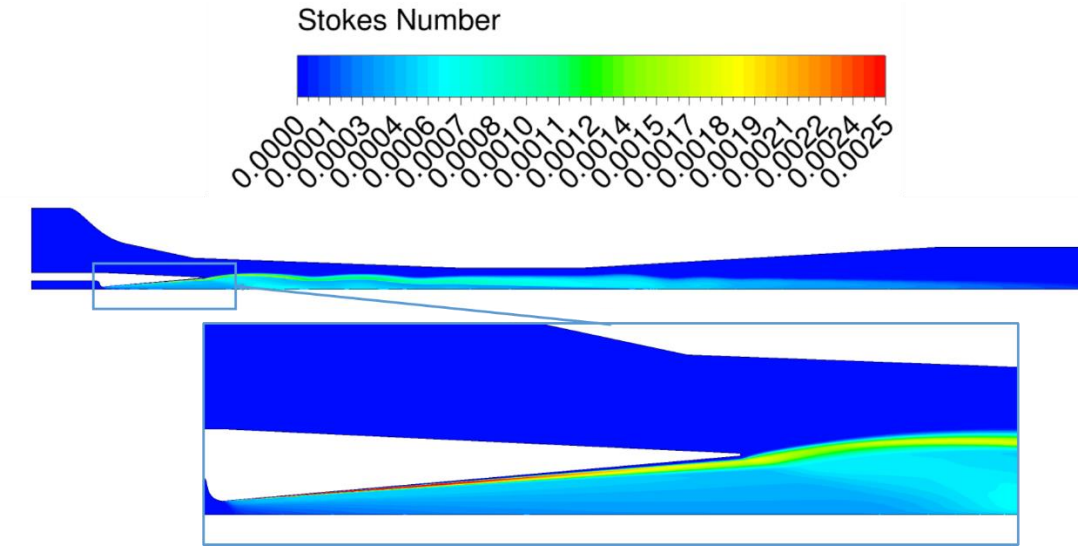

Fig. 16 – "Turbulent" Stokes number within the ejector (case with P_{out} = 4.2 kPa)

Finally, a last, key aspect that is of particular concern for steam ejector studies is related to the very low temperature levels attained by the expanding stream. This problem is particularly critical for ejector refrigeration applications, where efficiency considerations impose the use of low or no level of superheating at the inlet of the motive stream (this is also the case for the experimental results used in this work). Consequently, the motive jet can reach temperature levels that go well below the triple point, causing the possible appearance of ice.

Fig. 17 shows the mixture temperature contour within the ejector. Clearly, the temperature goes well below the limit of the triple point and the presence of ice cannot be excluded (especially downstream of the nozzle exit plane where the mixture temperature reaches values close to 210 K). Nevertheless, ice crystal formation, in much the same way as for droplet nucleation, is fundamentally a time dependent phenomenon and some degrees of supercooling usually exists before the water vapor or liquid starts to solidify.

In particular, experiments in cloud chambers with pure water vapor indicates that the homogeneous nucleation of ice usually occurs with around 30-40 K of supercooling [40]. By contrast, recent investigations in supersonic nozzles have shown that for the high cooling rates and small cluster sizes that are achieved in these devices, the supercooling can be as high as 90 K (i.e., supercooled water temperatures of nearly 190 K) [41]. However, these tests were conducted with ultrapure water and may not be directly applicable to the present study (this is

because impurities in the water droplets or vapor stream can greatly anticipate crystal formation). As a result, the presence of ice cannot be excluded in the steam ejector under investigation.

The appearance of water ice crystal may induce substantial modifications to the mixture flow behavior. For instance, the change in the latent heat release (from the value of condensation to that of solidification) may modify the nozzle Mach and pressure profiles. Moreover, phenomena such as crystals agglomeration and deposition may be important and could lead to modifications in the ejector geometrical profiles. On the other hand, the presence of shocks immediately after every steam expansion may lead to the sudden melting of the ice, limiting its impact on the global flow dynamics. In this case, numerical simulations may still incur in significant discrepancies due to the uncertain extrapolation of the supercooled water properties below the triple point temperature (most of these, including viscosity, specific heat, surface tension and others, present exponential variations with decreasing temperatures [40]). In view of these many aspects, it is important that future experimental investigations properly address the analysis of ice formation inside steam ejectors.

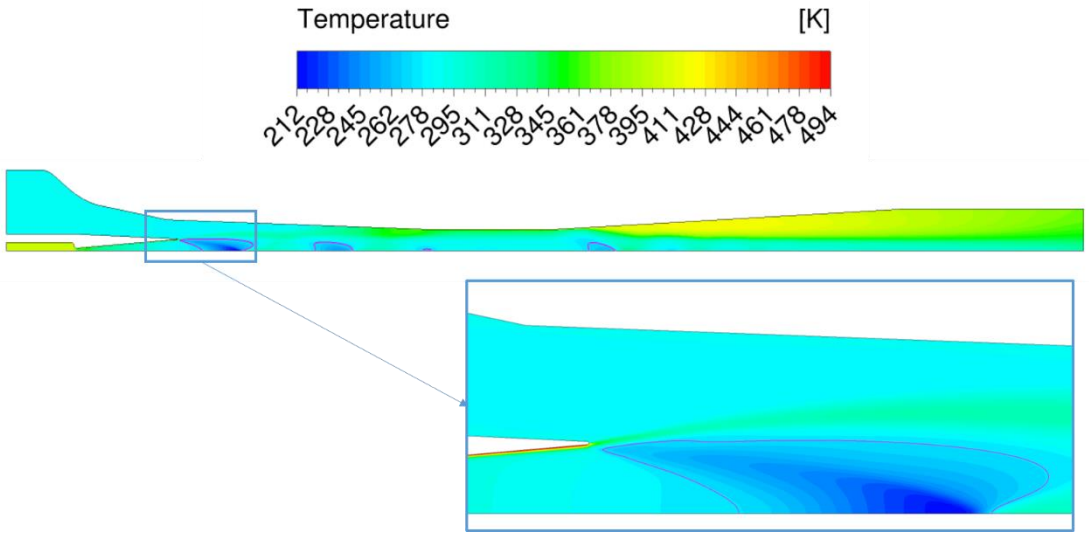

Fig. 17 – Temperature trend along the ejector; in purple is the line corresponding to the triple point temperature (case with P_{out} = 4.2 kPa)

5. Concluding remarks

A numerical model for the simulation of wet-steam flow has been developed and implemented within the CFD software ANSYS Fluent via User Defined Functions. This approach allows great flexibility in the choice of the physical model settings and calibration parameters.

The model has been tested against experimental data from a De-Laval nozzle and a steam ejector test-case. The nozzle simulations have shown that the developed model can produce results that substantially agree with experiments and that are in line with those provided by the ANSYS Fluent wet steam model. However, the model improves on the Fluent built-in scheme by providing a proper conservation of the number of droplets within the computational domain. The analysis of the sensitivity to changes in model settings has shown the importance of both the nucleation rate non-isothermal correction and droplet growth law in predicting the

condensation starting position. By contrast, the adoption of the IAPWS correlation for the surface tension did not result in any detectable difference with respect to the formulation used in the present model.

Simulations for the steam ejector test case have demonstrated a substantial agreement with experiments, both in terms of mass flow rates and wall pressure profiles. Some discrepancies are found for the primary mass flow rate that probably stems from the presence of liquid at the nozzle inlet or from uncertainties in the nozzle throat dimensions. The entrainment of the secondary flow can also be reproduced with accuracy, as long as the effects of compressibility on mixing layer development are accounted for in the turbulence model.

The analysis of the internal flow features has shown that, due to high level of expansion of the primary jet, the liquid mass fraction reaches values up to 20% within the mixing chamber. In this region, the mixture temperature goes well below the water triple point, indicating the possible presence of ice. However, the limited residence time and the presence of shocks may limit the impact of ice formation on the flow dynamics.

The assessment of the Knudsen and Stokes numbers within the ejector suggests that the approximations of free molecular droplet growth regime and velocity equilibrium between the phases should be valid, at least in the flow regions away from dynamic shocks.

In conclusion, it is important to note that some of the most important limitations of the model are related to the assumption of the flat-film surface tension as well as to the absence of a sink term in the droplets number equation. Improvements in both these two aspects may greatly increase the prediction capability of the wet-steam model but require an extensive development and tuning process that will be the subject of future studies.

References

[1] P. P. Wegener and L. M. Mack, "Condensation in Supersonic Wind Tunnels," in *Advances in Apllied Mechanics*, New York, Academic Press Inc., 1958, pp. 307-440.

[2] P. G. Hill, "Condensation of water vapour during supersonic expansion in nozzles," *J. Fluid Mech.*, vol. 25, no. 3, pp. 593-620, 1966.

[3] J. Starzmann, F. R. Huges, A. J. White, J. Halama, V. Hric, M. Kolovratnik, H. Lee, L. Sova, M. Statny, S. Schuster, M. Grubel, M. Schatz, D. M. Vogt, P. Y., G. Patel, T. Turunen-Saaresti, V. Gribin, V. Tishchenko, I. Garilov and e. al., "Results of the International Wet Steam Modelling Project," Prague, 2016.

[4] T. Sriveerakul, S. Aphornratana and K. Chunnanond, "Performance prediction of steam ejector using computational fluid: Part 1. Validation of the CFD results," *International Journal of Thermal Sciences*, vol. 46, pp. 812-822, 2007.

[5] K. Ariafar, D. Buttsworth and G. Al-Doori, "Effect of mixing on the performance of wet steam ejectors," *Energy*, vol. 93, pp. 2030-2041, 2015.

[6] X. Wang, L. H.J., D. J.L. and T. J.Y., "The spontaneously condensing phenomena in a steam-jet pump and its influence," *International Journal of Heat and Mass Transfer*, vol. 55, p. 4682–4687, 2012.

[7] K. Chunnanond and S. Aphornratana, "An experimental investigation of a steam ejector," *Applied Thermal Engineering*, vol. 24, pp. 311-322, 2004.

[8] C. A. Moses and G. D. Stein, "On the growth of steam droplets formed in a Laval nozzle using both static pressure and light scattering measurements," *Journal of Fluids Engineering,* pp. 311-322, 1978.

[9] G. Al-Doori, Investigation of Refrigeration System Steam Ejector Performance Through Experiments and Computational Simulations, Ph.D. thesis, University of Southern Queensland, 2013.

[10] F. Giacomelli, G. Biferi, F. Mazzelli and A. Milazzo, "CFD modeling of supersonic condensation inside a steam ejector," *Energy Procedia,* no. 101, pp. 1224-1231, 2016.

[11] A. Gerber and M. Kermani, "A pressure based Eulerian-Eulerian multiphase model for non-equilibrium condensation in transonic steam flow," *International Journal of Heat and Mass Transfer,* pp. 2217-2231, 2004.

[12] W. Wróblewski, S. Dykas and A. Gepert, "Steam condensing flow modeling in turbine channels," *International Journal of Multiphase Flow,* vol. 35, pp. 498-506, 2009.

[13] S. Dykas and W. Wróblewski, "Single- and two-fluid models for steam condensing flow modeling," *International Journal of Multiphase Flow,* vol. 37, pp. 1245-1253, 2011.

[14] C. Brennen, Cavitation and Bubble Dynamics, Oxford University Press, 1995.

[15] F. Bakhtar, J. B. Young, A. J. White and D. A. Simpson, "Classical nucleation theory and its application to condensing steam flow calculations," in *Proceedings of the Institution of Mechanical Engineers, Part C: Journal of Mechanical Engineers Science*, 2005.

[16] A. Kantrovitz, "Nucleation in very rapid vapour expansions," *J. Chem. Phys.*, vol. 19, pp. 1097-1100, 1951.

[17] F. Mazzelli, Single & Two-Phase Supersonic Ejectors for Refrigeration Applications, Florence: Ph.D. Thesis, 2015.

[18] J. B. Young, "The Spontaneous Condensation in Supersonic Nozzles," *PhysicoChemical Hydrodynamics,* vol. 3, no. 1, pp. 57-82, 1982.

[19] International Assotiation for the Properties of Water and Steam, "Thermophysical Properties of Metastable Steam and Homogeneous Nucleation," 2011.

[20] J. B. Young, "An Equation of State for Steam for Turbomachinery and Other Flow Calculations," *Journal of Engineering for Gas Turbines and Power,* vol. 110, no. 1, pp. 1-7, 1988.

[21] E. Lemmon, M. Huber and M. McLinden, "NIST Standard Reference Database 23: Reference Fluid Thermodynamic and Transport Properties-REFPROP, Version 9.1," 2013.

[22] ANSYS Inc., ANSYS Fluent Theory Guide, Canonsburg, PA: release 18.0, 2016.

[23] M. Labois and C. Narayanan, "Non-conservative pressure-based compressible formulation for multiphase flows with heat and mass transfer," in *9th International Conference on Multiphase Flow*, May 22nd - 27th, Firenze, Italy, 2016.

[24] L. Zori and F. Kelecy, "Wet Steam Flow Modeling in a General CFD Flow Solver," in *35th AIAA Fluid Dynamics Conference and Exhibit*, Toronto, Ontario, Canada, 6 - 9 June 2005.

[25] Y. Yang and S. Shen, "Numerical simulation on non-equilibrium spontaneous condensation," *International Communications in Heat and Mass Transfer ,* vol. 36, pp. 902-907, 2009.

[26] B. Leonard, "A stable and accurate convective modelling procedure based on quadratic upstream interpolation," *Computer Methods in Applied Mechanics and Engineering,* vol. 19, pp. 59-98, 1979.

[27] G. Gyarmathy, "Bases for a theory for wet steam turbines," PhD thesis, ETH Zurich, 1962.

[28] M. Joswiak, N. Duff, M. Doherty and B. Peters, "Size-Dependent Surface Free Energy and Tolman-Corrected Droplet Nucleation of TIP4P/2005 Water," *J. Phys. Chem. Lett.* , vol. 4, p. 4267−72, 2013.

[29] F. R. Menter, "Two-Equation Eddy-Viscosity Turbulence Models for Engineering Applications," *AIAA Journal,* vol. 32, no. 8, pp. 1598-1605, 1994.

[30] F. Mazzelli, A. B. Little, S. Garimella and Y. Bartosiewicz, "Computational and Experimental Analysis of Supersonic Air Ejector: Turbulence Modeling and Assessment of 3D Effects," *International Journal of Heat and Fluid Flow,* vol. 56, pp. 305-316, 2015.

[31] F. Mazzelli and A. Milazzo, "Performance analysis of a supersonic ejector cycle," *International Journal of Refrigeration,* vol. 49, pp. 79-92, 2015.

[32] F. Hughes, J. Starzmann, A. White and Y. J.B., "A Comparison of Modeling Techniques for Polydispersed Droplet Spectra in Steam Turbines," *Journal of Engineering for Gas Turbines and Power,* vol. 138, 2016.

[33] H. Ikawa, Turbulent Mixing Layer in Supersonic Flow, Ph.D. thesis, California Institute of Technology, 1973.

[34] G. Brown and A. Roshko, "On density effects and large structure in turbulent mixing layers," *journal of Fluid Mechanics* , vol. 64, pp. 775-816, 1974.

[35] A. Smits and J.-P. Dussauge, Turbulent Shear Layers in Supersonic Flow, second edition, New York, NY: Springer, 2006.

[36] T. Gatsky and J.-P. Bonnet, Compressibility, Turbulence and High Speed Flow, 2nd edition, Oxford, UK.: Academic Press, 2013.

[37] D. Wilcox, "Dilatation–dissipation corrections for advanced turbulence models," *AIAA Journal,* vol. 11, pp. 2639-2646, 1992.

[38] D. Wilcox, Turbulence Modeling for CFD, La Canada, California: DCW Industries, Inc, 2006.

[39] C. Crowe, J. Schwarzkopf, M. Sommerfeld and Y. Tsuji, Multiphase flows with droplets and particles, second edition, Boca Raton, FL: CRC Press, 2012.

[40] H. R. Pruppacher, "A new look at homogeneous ice nucleation in supercooled water drops," *J. Atmos. Sci.* , vol. 52, pp. 1924-33, 1995.

[41] J. Wölk, B. Wyslouzil and R. Strey, "Homogeneous nucleation of water: From vapor to supercooled droplets to ice," *AIP Conf. Proc.,* vol. 1527, pp. 55-62, 2013.

[42] The International Association for the Properties of Water and Steam, "Revised Release on Surface Tension of Ordinary Water Substance," IAPWS report, 2014.

1126
1127